Electron−Phonon and Spin−Lattice Coupling in Atomically Thin Layers of MnBi$_2$Te$_4$

Jeongheon Choe,[#] David Lujan,[#] Martin Rodriguez-Vega,* Zhipeng Ye, Aritz Leonardo, Jiamin Quan, T. Nathan Nunley, Liang-Juan Chang, Shang-Fan Lee, Jiaqiang Yan, Gregory A. Fiete, Rui He,* and Xiaoqin Li*

Read Online

ACCESS | Metrics & More | Article Recommendations | SI Supporting Information

ABSTRACT: MnBi$_2$Te$_4$ represents a new class of magnetic topological insulators in which novel quantum phases emerge at temperatures higher than those found in magnetically doped thin films. Here, we investigate how couplings between electron, spin, and lattice are manifested in the phonon spectra of few-septuple-layer thick MnBi$_2$Te$_4$. After categorizing phonon modes by their symmetries, we study the systematic changes in frequency, line width, and line shape of a spectrally isolated A$_{1g}$ mode. The electron−phonon coupling increases in thinner flakes as manifested in a broader phonon line width, which is likely due to changes of the electron density of states. In 4- and 5-septuple-thick samples, the onset of magnetic order below the Néel temperature is concurrent with a transition to an insulating state. We observe signatures of a reduced electron−phonon scattering across this transition as reflected in the reduced Fano parameter. Finally, spin−lattice coupling is measured and modeled from temperature-dependent phonon frequency.
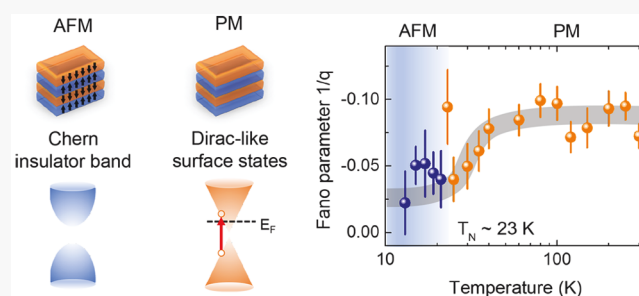
The interplay between topology and magnetic order can lead to exotic quantum phases and phenomena such as quantized anomalous Hall effect, axion insulators, and Majorana modes.[1,2] While magnetically doped thin films have been previously investigated, topological materials with intrinsic magnetic order, in particular, van der Waals MnBi$_{2n}$Te$_{3n+1}$ compounds, have only been realized recently and found to host novel quantum phases at elevated temperatures.[3−8] Within this family, MnBi$_2$Te$_4$ (MBT) has been most extensively investigated using transport measurements,[9,10] angle-resolved photoemission spectroscopy,[3,5,11−13] and magnetic circular dichroism measurements.[14,15]

In the high temperature paramagnetic phase, bulk MBT is a topological insulator with gapless Dirac-like surface states.[4,11] Below the magnetic transition temperature, MBT is a topological antiferromagnetic (AFM) insulator with gapped surface states and $Z_2 = 1$,[3] according to the Z_2 classification.[16] The Néel temperature ∼20−24 K has been determined from transport measurements in both the bulk and thin film limit.[9,10,15,17]

The topological and magnetic properties of MBT have been predicted to depend on the number of septuple-layers (SLs).[18−20] While it is easy to confirm the layer-dependent magnetic orders, there are still debates on whether odd- and even layer MBT in the few-layer thick range may host different types of

topological insulators (e.g., Axion or Chern insulators)[9,10,15,21] or how electronic topology couples to the magnetic order. Many compelling properties of magnetic topological materials originate from the gapped electron surface states that are protected by discrete symmetry. Electron−phonon interaction is believed to be the main scattering mechanism for such surface states at finite temperature.[22] Such coupling in other topological materials has been studied via temperature-dependent Dirac Ferminon quasiparticle self-energy obtained from ARPES measurements.[23−25] However, performing such measurements in a layer-thickness-dependent manner would be very challenging. Thus, it is important to explore alternative measurements to quantify such coupling, especially in the ultrathin thickness limit.

Here, we study how couplings between electron, spin, and lattices are manifested in phonon spectra of few-layer thick MBT. Combining polarization-resolved Raman spectroscopy
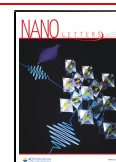
measurements, group theory, and density functional theory (DFT), we categorize phonon modes by their symmetries. A clear thickness-dependent frequency shift is observed for all phonon modes. We focus on a spectrally isolated A_{1g} mode and find the electron−phonon interaction increases as manifested in a broader linewidth in thinner samples. We analyze the temperature-dependent frequency, line shape, line width and intensity of the A_{1g} mode of the 4- and 5-SLs carefully. Electron−phonon coupling is quantified by the Fano parameter $1/q$ and found to be larger in the paramagnetic phase than that in the insulating AFM phase below the Néel temperature. By fitting the temperature-dependent frequency shift above the Néel temperature with an anharmonic phonon model, we quantify the spin−lattice coupling. Our studies provide evidence of coupled electron, lattice, and spin degrees of freedom in few-layer MBT and, consequently, different electron−phonon scatterings across the magnetic transition temperature.

The crystal structure of MBT consists of seven atomic layers (Te−Bi−Te−Mn−Te−Bi−Te) stacked along the c-direction (Figure 1a). The adjacent SLs are bonded by van der Waals
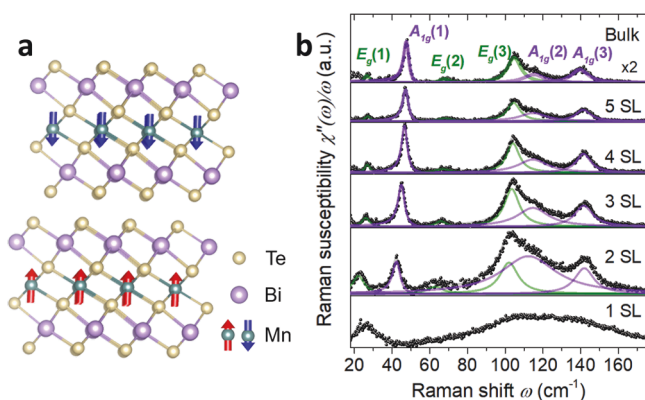

Figure 1. Schematics of $MnBi_2Te_4$ lattice and spin configuration in the AFM phase and room temperature layer-dependent Raman susceptibility. (a) Schematic of layered crystal structure with A-type antiferromagnetic order. The 1-septuple layer (SL) consists of the magnetic Mn^{2+} ions and the surrounding Te−Bi−Te layers, known to be topological insulators when isolated. (b) Layer-dependent Raman susceptibility of $MnBi_2Te_4$. Data were taken at room temperature with collinear polarization. Black dots are raw data points. Solid curves are fits using the Fano function. A quasielastic scattering background was subtracted. Horizontal lines represent zero intensity. The bulk spectrum is magnified by a factor of 2. Colors: violet, A_{1g} mode; green, E_g mode.

forces, and can be cleaved along the (001) surface terminated at Te atoms. The topological properties originate from the Bi and Te layers while the magnetic Mn^{2+} ion layer is responsible for the long-range spin ordering. The Mn^{2+} ions possess a large magnetic moment of ideally ∼5 bohr magnetons. Below the Néel temperature, MBT exhibits an A-type AFM phase, with spins aligned perpendicular to the 2d planes.[17] Spins within a layer are aligned in parallel, while spins between adjacent layers are antiparallel. The net magnetization in even-number layers is zero but uncompensated in odd-number layers.

We first measured room-temperature Raman spectra of few-layer MBT and observed clear thickness-dependent phonon modes (Figure 1b). The atomically thin MBT flakes were exfoliated onto a silicon wafer using an Al_2O_3-assisted exfoliation technique[9] (see Methods and thickness character-

ization in Supplementary Note A). We observed 6 different phonon peaks at room temperature and assigned these modes corresponding to their symmetry class based on polarization-dependent measurements in combination with a symmetry analysis (presented in ref.[26] and Supplementary Notes B and C). The A_{1g} (E_g) modes correspond to those with atoms vibrating in the out-of-plane (in-plane) direction. After applying the Bose factor correction, we model the quasi-elastic scattering background to obtain the Raman susceptibility (see details in the Supplementary Note H). All phonon modes are fitted with a general Fano line shape after removing the quasi-elastic background,[27]

$$I(\omega) = I_0 \frac{[q + (\omega - \omega_0)/\Gamma]^2}{1 + [(\omega - \omega_0)/\Gamma]^2} \tag{1}$$

In addition to the central frequency ω_0, the line shape is quantified by the Fano parameter[28,29] $1/q = \pi V \varrho(E)/([T_p/T_e + VR(E)])$, and the phonon line width $\Gamma = \pi V^2 \varrho(E)$. $\varrho(E)$ is the electronic density of states with respect to the Fermi energy, V is the electron−phonon interaction, $T_e(T_p)$ is the Raman matrix element between the ground and excited electronic (phononic) states, and $R(E) = \mathrm{Re}[G(E)]$ corresponds to the real part of the N-SL MBT Green's function $G(E)$ (details in the Supplementary Note E). By using this simple model to analyze the measured Raman spectra, we have assumed an averaged value for electronic Raman matrix element T_e and its coupling to the phonon state near the Fermi level. While the Fermi level is ∼280 meV in the bulk based on the ARPES measurements on the same batch of samples,[30] the Fermi level is unknown in the thin flakes. We have assumed that the Fermi level is nearly independent of the layer thickness and close to the conduction band edge based on recent experiments on other MBT thin films.[31]

The extracted phonon frequencies and line widths of all the phonon modes for 2-SLs to 5-SLs are summarized in the Supporting Information Table 2, along with the calculated phonon frequencies (see Supplementary Note D). The bulk MBT Raman spectra are also measured and analyzed to provide a comparison to those taken on thin layers. The calculated phonon modes allow us to associate the observed Raman modes with particular lattice vibrations.[26] The Raman modes from 1-SL sample are significantly broadened possibly due to disorder or interactions with the substrate. The Raman spectra from 2-SLs to bulk show well-defined phonon modes with decreasing line widths for thicker layers. The frequency of four low frequency phonon modes (i.e., E_g(1−3) and A_{1g}(1)) softens with decreasing layer number. This softening can be explained with a simple chain model of coupled atoms with more than one atom in a unit cell and layer-thickness-dependent van der Waals coupling.[32−34] In the Supplementary Note F, we provide details for the DFT calculations.

A symmetry analysis of the electronic bands reveals states with both A_{1g} and E_g representations at the Γ point. Therefore, from the symmetry point of view, both A_{1g} and E_g phonon modes can couple to electronic transitions. We focus on a spectrally isolated A_{1g}(1) mode (Figure 2a) that corresponds to Bi and Te atoms vibrate along the out-of-plane direction (Figure 2b). We summarize its frequency and line width as a function of thickness in Figure 2c. The frequency change (green) is modeled by a linear chain model that has been used in previous experiments.[32−34] A broader phonon line width in thinner flakes (purple) provide evidence for layer-thickness-
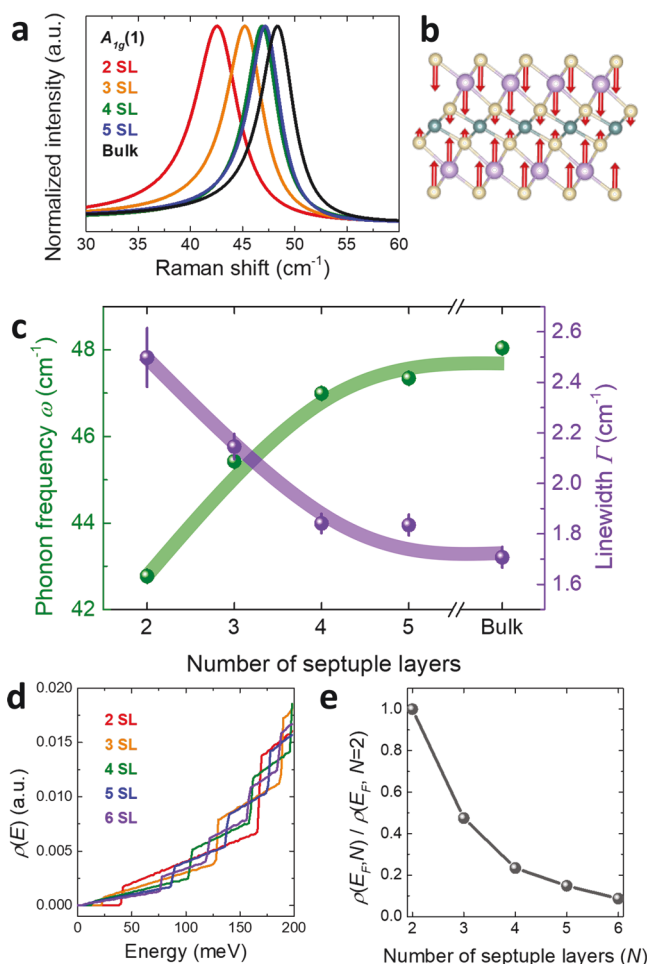
Figure 2. Layer number dependence of the electron–phonon interaction in the paramagnetic phase. (a) Fano resonance fits of the $A_{1g}(1)$ mode. The peak intensity is normalized. (b) Illustration of corresponding atomic displacement. (c) Thickness dependence of the $A_{1g}(1)$ mode frequency and line width. The color solid lines are guides to the eye. (d) Calculated electron density of states as a function of energy E. (e) Calculated electron density of states at E_F as a function of layer number N. E_F is located near the conduction band edge (CBE).

dependent electron–phonon interaction in MBT, similar to another recent report on topological materials.[35] This thickness-dependent electron–phonon interaction may originate from increased density of states at the Fermi energy, $\varrho(E_F)$ shown in Figure 2d,e. This calculation is based on the low-energy model described in the Supplemental Note E.[20]

Next, we focus on the temperature dependence of the Raman spectra from the 4- and 5-SLs because many quantum transport measurements revealing exotic electronic phases were reported in this thickness range.[9,10] Comparing Raman spectra taken below the Néel temperature and at room temperature may reveal the possible interplay between magnetic ordering and phonons. In the AFM phase ($T = 13$ K), phonon frequencies are blue-shifted, and the phonon line width becomes narrower compared to those in the paramagnetic (PM) phase ($T = 300$ K) (Figure 3a). Figure 3b shows the full temperature dependence of the Fano parameter $1/q$. The line shape evolves from asymmetric to symmetric shape as the temperature decreases. Correspondingly, the Fano parameter $1/q$ approaches zero, indicating that electron–

phonon coupling reduces. Analogously, reduction of the electron–phonon coupling was previously reported in a rare-earth titanite series $RTiO_3$ across a metal-to-insulator transition,[36] and in $LiOsO_3$ across a ferroelectric transition.[37]

The asymmetric Fano line shape originates from the quantum interference between the electron continuum and the discrete phonon mode. The negative Fano parameter of the $A_{1g}(1)$ phonon corresponds to a constructive (destructive) interference between the discrete phonon and the electron continuum on the low-energy (high-energy) side of the resonance. Specifically, the $A_{1g}(1)$ mode couples to electronic transitions near the Fermi level (E_F). In the paramagnetic phase, MBT has surface states (gapless or a small gap) with a Dirac-like dispersion centered at the Γ point. The electron continuum below E_F is excited during the phonon decay processes. Below the Néel temperature ($\sim$23 K), the AFM phase breaks time-reversal symmetry and increases the gap of the electronic states (Figure 3d). In the insulating phase, electron–phonon scattering is reduced as the gap impedes phonon-mediated electron transitions, which is manifested in the reduced Fano parameter below the Néel temperature in both 4- and 5-SL samples as shown in Figure 3b. Fano line shape is often attributed to electron–phonon interaction.[27,38]

Concurrent with the changes of the Fano parameter as a function of temperature, we also observe that the line width and the integrated intensity of the $A_{1g}(1)$ mode in the 4- and 5-SLs evolve in a qualitatively similar way (Figure 3c). The temperature dependence of both the line widths and intensity are well-described by the anharmonic decay model.[39] A similar temperature dependence of line widths has been reported in thin-film Bi_2Te_3,[40] which was attributed to phonon–phonon interaction. In other topological materials (e.g., Weyl semimetals NbAs and TaAs), however, the deviation from the anharmonic decay model was observed and attributed to electron–hole pair excitations near the Fermi level.[41,42] Future investigations of MBT compounds with controllable doping may reveal rich phenomena such as excitation-energy-dependent Raman spectra.

We now analyze spin–phonon coupling strength associated with the $A_{1g}(1)$ mode. Above the Néel temperature, the temperature-dependent phonon frequency (Figure 4a) is determined by anharmonic effects, i.e., phonon–phonon scattering.[40] The data above the transition temperature ($T > 23$ K) is fitted to $\omega_p(T) = \omega_p(0) - A\left(1 + \frac{2}{\exp[x] - 1}\right)$, where $\omega_p(0)$ is the zero-temperature phonon frequency, A is a coefficient related to the 3-phonon scattering strength, and $x = \frac{\hbar\omega_p(0)}{2k_BT}$ with Planck's constant $\hbar$ and Boltzmann's constant k_B. In the magnetically ordered state ($T < 23$ K), spin–lattice coupling shifts the phonon frequency. The phonon frequencies deviate from the anharmonic model, $\omega_p{'} = \omega_p(T) + \Delta\omega_{sp}$ quantifies this coupling. We extract the spin–phonon interaction strength δ_{sp} using a modified mean-field model $\Delta\omega_{sp}(T < T_N) = \frac{\delta_{sp}}{2\mu\omega_p(0)}\left(1 - \frac{T}{T_N}\right)$ where μ is the mode reduced mass (Figure 4b). Using this modified mean-field model, one can compare spin–lattice coupling between different phonon modes. The spin–lattice coupling δ_{sp} extracted from the 4- and 5-SL sample is 0.8 ± 0.2 meV/Å^2 and 1.7 ± 0.4 meV/Å^2, respectively. A larger spin–lattice coupling in the 5-SL sample is reasonable considering it has a net magnetic moment. The further details of the modified
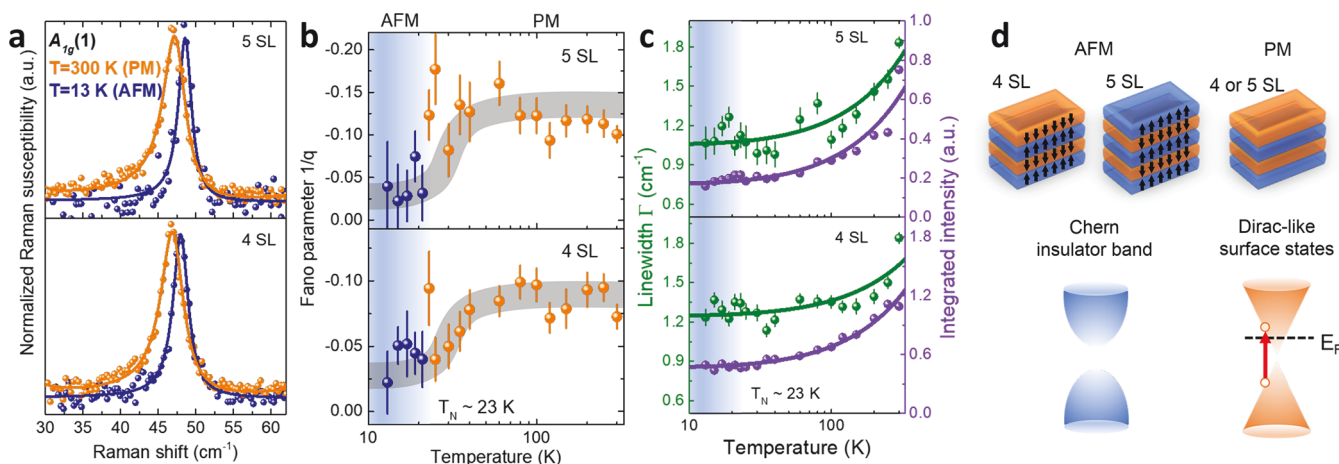
Figure 3. Temperature dependence of the $A_{1g}(1)$ phonon mode in 4- and 5-SLs of $MnBi_2Te_4$. (a) Normalized Raman susceptibility in the AFM (13 K) and the PM (300 K) phase. Solid lines are Fano resonance fits. (b) Fano parameter $1/q$ as a function of temperature. The Néel temperature (T_N) is ~23 K for both 4- and 5-SLs. The gray curves are guides to the eye. (c) Temperature dependence of line width and integrated intensity. The solid curves are anharmonic decay model fits. (d) Schematic illustration of the magnetic configurations with corresponding electronic structures confirmed by previous transport measurements. The red arrow represents the electronic transition with the same energy as the $A_{1g}(1)$ mode.
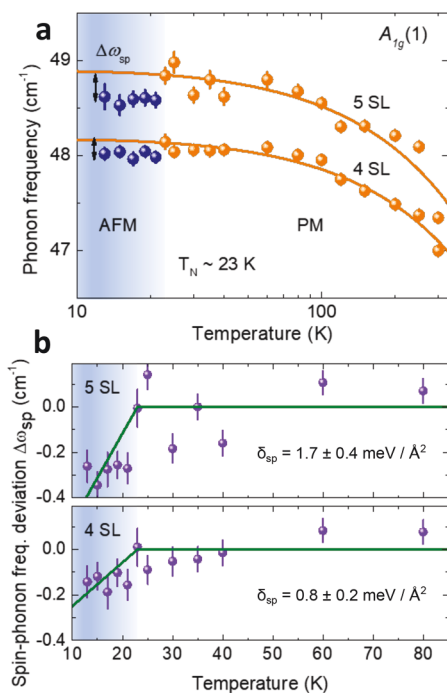

Figure 4. Spin−phonon coupling in 4- and 5-SLs of $MnBi_2Te_4$. (a) Temperature dependence of $A_{1g}(1)$ phonon frequencies. The solid curves are anharmonic fitting models. The black arrows represent the deviation from the anharmonic curve ($\Delta\omega_{sp}$), which reflects the corresponding spin−phonon coupling strength. (b) Spin−phonon frequency deviation $\Delta\omega_{sp}$ as a function of temperature. The mean-field model (solid line) is applied to extract the spin−phonon coupling strength δ_{sp}.

mean-field theory are explained in supplementary Note G. The frequency shift characterizing the spin−lattice coupling is proportional to the phonon frequency shift itself. The frequency shift (~0.3%) in MBT is comparable to that in other vdW magnets, e.g., $Cr_2Ge_2Te_6$.[43] Although the frequency shift is small, it is nevertheless a robust observation. If we fit all data points using the anharmonic model (i.e., including those

below the Néel temperature), we would obtain a larger fitting error. (Supplementary Note I)

In summary, we investigate how different degrees of freedom couple to each other in few-layers thick $MnBi_2Te_4$ and how these couplings are manifested in the phonon spectra, particularly the $A_{1g}(1)$ mode. Our studies provide significant new insight compared to a previous Raman experiment that was performed on a thick MBT sample to confirm a lack of structural change as a function of temperature.[14] While the mechanisms that contribute to Raman spectral features (e.g., line shape and line width) can be complex, analyzing their changes as a function of layer thickness and temperature reveal intrinsic properties of MBT. There are several main findings. First, Raman spectra show a strong layer-thickness dependence. Changes in the electron density of states lead to stronger electron−phonon coupling as the thickness reduces. Second, electron−phonon scattering is reduced across the Néel temperature likely because the magnetic ordering modifies the gap below the Néel temperature. Third, we quantify spin−lattice coupling via phonon-frequency deviation from an anharmonic phonon model. The temperature-dependent changes in electron−phonon scattering and the spin−lattice coupling are stronger in the 5-SL sample, which has a net magnetic moment below the Néel temperature. Since the precise electron−phonon coupling strength may depend on the Fermi-level, we theoretically explored the influence of a different Fermi level and found that an increasing density of states in thinner layers provides a plausible explanation for increasing electron−phonon interaction. In the future, a systematic study of how the Raman line shape evolves as a function of doping density would be very informative.

■ METHODS

Sample Preparation. $MnBi_2Te_4$ (MBT) crystals were grown by the flux method.[17] The Al_2O_3 film was deposited on a freshly cleaved surface of a bulk crystal using an e-beam evaporator.[9,44] The MBT/Al_2O_3 stack was exfoliated down the few-layer thickness using a thermal release tape. The MBT/Al_2O_3 stack was released on a transparent PDMS stamp upon heating. We performed optical transmittance measurements to

determine the layer thickness based on the Beer–Lambert law.[9] Finally, The PDMS stamp with MBT/Al_2O_3 the layers was transferred onto a SiO_2/Si chip. To avoid possible environmental damage to sample, we performed procedure above in a glovebox. We mounted the sample in the cryostat, and immediately pumped down the cryostat to minimize exposure to ambient environment for less than a minute.

Raman Spectroscopy. Raman measurements were performed using a 632.81 nm excitation laser with a full-width-half-maximum (fwhm) of 0.85 cm^{-1}. The laser power was kept at ~100 μW to avoid local heating and damage to the samples. The laser beam was focused onto the sample via a 40× microscope objective lens to a spot size of about 3 μm in diameter. The Raman signal was collected in the backscattering geometry. Following a Horiba LabRAM HR Evolution Raman microscope (1800 grooves/mm grating), the signal was detected with a thermoelectrically cooled CCD. All measurements were taken in a closed-cycle helium cryostat from 10 to 300 K with a base pressure lower than 7×10^{-7} Torr.

■ ASSOCIATED CONTENT

ⓈⒾ Supporting Information

The Supporting Information is available free of charge at https://pubs.acs.org/doi/10.1021/acs.nanolett.1c01719.

> Layer thickness identification, symmetry analysis, polarization dependence of Raman spectra, layer dependence of phonon frequencies, line widths, and Fano parameter, electron–phonon interactions, density functional theory calculation details, spin–phonon coupling, Bose correction and quasielastic scattering background, reduced χ^2 of anharmonic fitting method (PDF)

■ AUTHOR INFORMATION

Corresponding Authors

Martin Rodriguez-Vega − *Theoretical Division, Los Alamos National Laboratory, Los Alamos, New Mexico 87545, United States;* ⓞ orcid.org/0000-0001-8929-6546; Email: rodriguezvega@lanl.gov

Rui He − *Department of Electrical and Computer Engineering, Texas Tech University, Lubbock, Texas 79409, United States;* ⓞ orcid.org/0000-0002-2368-7269; Email: rui.he@ttu.edu

Xiaoqin Li − *Department of Physics, Center of Complex Quantum Systems, The University of Texas at Austin, Austin, Texas 78712, United States; Center for Dynamics and Control of Materials, The University of Texas at Austin, Austin, Texas 78712, United States; Texas Materials Institute, University of Texas at Austin, Austin, Texas 78712, United States;* Email: elaineli@physics.utexas.edu

Authors

Jeongheon Choe − *Department of Physics, Center of Complex Quantum Systems, The University of Texas at Austin, Austin, Texas 78712, United States; Center for Dynamics and Control of Materials, The University of Texas at Austin, Austin, Texas 78712, United States*

David Lujan − *Department of Physics, Center of Complex Quantum Systems, The University of Texas at Austin, Austin, Texas 78712, United States; Center for Dynamics and Control of Materials, The University of Texas at Austin, Austin, Texas 78712, United States*

Zhipeng Ye − *Department of Electrical and Computer Engineering, Texas Tech University, Lubbock, Texas 79409, United States*

Aritz Leonardo − *Donostia International Physics Center, 20018 San Sebastian, Spain; Department of Physics, University of the Basque Country UPV/EHU, 48940 Leioa, Spain*

Jiamin Quan − *Department of Physics, Center of Complex Quantum Systems, The University of Texas at Austin, Austin, Texas 78712, United States*

T. Nathan Nunley − *Department of Physics, Center of Complex Quantum Systems, The University of Texas at Austin, Austin, Texas 78712, United States*

Liang-Juan Chang − *Department of Physics, The University of Texas at Austin, Austin, Texas 78712, United States; Institute of Physics, Academia Sinica, Taipei 11529, Taiwan*

Shang-Fan Lee − *Institute of Physics, Academia Sinica, Taipei 11529, Taiwan;* ⓞ orcid.org/0000-0001-5899-7200

Jiaqiang Yan − *Materials Science and Technology Division, Oak Ridge National Laboratory, Oak Ridge, Tennessee 37831, United States*

Gregory A. Fiete − *Department of Physics, Northeastern University, Boston, Massachusetts 02115, United States; Department of Physics, Massachusetts Institute of Technology, Cambridge, Massachusetts 02139, United States*

Complete contact information is available at:
https://pubs.acs.org/10.1021/acs.nanolett.1c01719

Author Contributions

[#]J.C. and D.L. contributed equally.

Notes

The authors declare no competing financial interest.

■ ACKNOWLEDGMENTS

■ REFERENCES

(1) Tokura, Y.; Yasuda, K.; Tsukazaki, A. Magnetic topological insulators. *Nat. Rev. Phys.* **2019**, *1*, 126−143.

(2) Liu, C.-X.; Zhang, S.-C.; Qi, X.-L. The Quantum Anomalous Hall Effect: Theory and Experiment. *Annu. Rev. Condens. Matter Phys.* **2016**, *7*, 301−321.

(3) Otrokov, M. M.; et al. Prediction and observation of an antiferromagnetic topological insulator. *Nature* **2019**, *576*, 416−422.

(4) Gong, Y.; et al. Experimental Realization of an Intrinsic Magnetic Topological Insulator*. *Chin. Phys. Lett.* **2019**, *36*, 076801.

(5) Hu, C.; et al. A van der Waals antiferromagnetic topological insulator with weak interlayer magnetic coupling. *Nat. Commun.* **2020**, *11*, 97.

(6) Hu, C.; et al. Realization of an intrinsic ferromagnetic topological state in $MnBi_8Te_{13}$. *Sci. Adv.* **2020**, *6*, No. eaba4275.

(7) Jahangirli, Z. A.; Alizade, E. H.; Aliev, Z. S.; Otrokov, M. M.; Ismayilova, N. A.; Mammadov, S. N.; Amiraslanov, I. R.; Mamedov, N. T.; Orudjev, G. S.; Babanly, M. B.; Shikin, A. M.; Chulkov, E. V. Electronic structure and dielectric function of Mn-Bi-Te layered compounds. *J. Vac. Sci. Technol., B: Nanotechnol. Microelectron.: Mater., Process., Meas., Phenom.* **2019**, *37*, 062910.

(8) Aliev, Z. S.; Amiraslanov, I. R.; Nasonova, D. I.; Shevelkov, A. V.; Abdullayev, N. A.; Jahangirli, Z. A.; Orujlu, E. N.; Otrokov, M. M.; Mamedov, N. T.; Babanly, M. B.; Chulkov, E. V. Novel ternary layered manganese bismuth tellurides of the $MnTe-Bi_2Te_3$ system: Synthesis and crystal structure. *J. Alloys Compd.* **2019**, *789*, 443−450.

(9) Deng, Y.; Yu, Y.; Shi, M. Z.; Guo, Z.; Xu, Z.; Wang, J.; Chen, X. H.; Zhang, Y. Quantum anomalous Hall effect in intrinsic magnetic topological insulator $MnBi_2Te_4$. *Science* **2020**, *367*, 895−900.

(10) Liu, C.; Wang, Y.; Li, H.; Wu, Y.; Li, Y.; Li, J.; He, K.; Xu, Y.; Zhang, J.; Wang, Y. Robust axion insulator and Chern insulator phases in a two-dimensional antiferromagnetic topological insulator. *Nat. Mater.* **2020**, *19*, 522−527.

(11) Chen, Y.; et al. Topological Electronic Structure and Its Temperature Evolution in Antiferromagnetic Topological Insulator $MnBi_2Te_4$. *Phys. Rev. X* **2019**, *9*, 041040.

(12) Hao, Y.-J.; et al. Gapless Surface Dirac Cone in Antiferromagnetic Topological Insulator $MnBi_2Te_4$. *Phys. Rev. X* **2019**, *9*, 041038.

(13) Vidal, R. C.; et al. Surface states and Rashba-type spin polarization in antiferromagnetic $MnBi_2Te_4(0001)$. *Phys. Rev. B: Condens. Matter Mater. Phys.* **2019**, *100*, 121104.

(14) Yang, S.; Xu, X.; Zhu, Y.; Niu, R.; Xu, C.; Peng, Y.; Cheng, X.; Jia, X.; Huang, Y.; Xu, X.; Lu, J.; Ye, Y. Odd-Even Layer-Number Effect and Layer-Dependent Magnetic Phase Diagrams in $MnBi_2Te_4$. *Phys. Rev. X* **2021**, *11*, 011003.

(15) Ovchinnikov, D.; et al. Intertwined Topological and Magnetic Orders in Atomically Thin Chern Insulator $MnBi_2Te_4$. *Nano Lett.* **2021**, *21*, 2544−2550.

(16) Mong, R. S. K.; Essin, A. M.; Moore, J. E. Antiferromagnetic topological insulators. *Phys. Rev. B: Condens. Matter Mater. Phys.* **2010**, *81*, 245209.

(17) Yan, J.-Q.; Zhang, Q.; Heitmann, T.; Huang, Z.; Chen, K. Y.; Cheng, J.-G.; Wu, W.; Vaknin, D.; Sales, B. C.; McQueeney, R. J. Crystal growth and magnetic structure of MnBi2Te4. *Phys. Rev. Mater.* **2019**, *3*, 064202.

(18) Li, J.; Li, Y.; Du, S.; Wang, Z.; Gu, B.-L.; Zhang, S.-C.; He, K.; Duan, W.; Xu, Y. Intrinsic magnetic topological insulators in van der Waals layered $MnBi_2Te_4$-family materials. *Sci. Adv.* **2019**, *5*, No. eaaw5685.

(19) Otrokov, M.; Rusinov, I.; Blanco-Rey, M.; Hoffmann, M.; Vyazovskaya, A.; Eremeev, S.; Ernst, A.; Echenique, P.; Arnau, A.; Chulkov, E. Unique Thickness-Dependent Properties of the van der Waals Interlayer Antiferromagnet $MnBi_2Te_4$ Films. *Phys. Rev. Lett.* **2019**, *122*, 107202.

(20) Lei, C.; Chen, S.; MacDonald, A. H. Magnetized topological insulator multilayers. *Proc. Natl. Acad. Sci. U. S. A.* **2020**, *117*, 27224−27230.

(21) Ge, J.; Liu, Y.; Li, J.; Li, H.; Luo, T.; Wu, Y.; Xu, Y.; Wang, J. High-Chern-number and high-temperature quantum Hall effect without Landau levels. *Natl. Sci. Rev.* **2020**, *7*, 1280−1287.

(22) Zhu, X.; Santos, L.; Howard, C.; Sankar, R.; Chou, F. C.; Chamon, C.; El-Batanouny, M. Electron-Phonon Coupling on the Surface of the Topological Insulator Bi_2Se_3 Determined from Surface-Phonon Dispersion Measurements. *Phys. Rev. Lett.* **2012**, *108*, 185501.

(23) Hatch, R. C.; Bianchi, M.; Guan, D.; Bao, S.; Mi, J.; Iversen, B. B.; Nilsson, L.; Hornekær, L.; Hofmann, P. Stability of the Bi_2Se_3(111) topological state: Electron-phonon and electron-defect scattering. *Phys. Rev. B: Condens. Matter Mater. Phys.* **2011**, *83*, 241303.

(24) Pan, Z.-H.; Fedorov, A. V.; Gardner, D.; Lee, Y. S.; Chu, S.; Valla, T. Measurement of an Exceptionally Weak Electron-Phonon Coupling on the Surface of the Topological Insulator Bi_2Se_3 Using Angle-Resolved Photoemission Spectroscopy. *Phys. Rev. Lett.* **2012**, *108*, 187001.

(25) Chen, C.; et al. Tunable Dirac Fermion Dynamics in Topological Insulators. *Sci. Rep.* **2013**, *3*, 2411.

(26) Rodriguez-Vega, M.; Leonardo, A.; Fiete, G. A. Group theory study of the vibrational modes and magnetic order in the topological antiferromagnet $MnBi_2Te_4$. *Phys. Rev. B: Condens. Matter Mater. Phys.* **2020**, *102*, 104102.

(27) Fano, U. Effects of Configuration Interaction on Intensities and Phase Shifts. *Phys. Rev.* **1961**, *124*, 1866−1878.

(28) Klein, M. V. In *Light Scattering in Solids I: Introductory Concepts*; Cardona, M., Ed.; Springer Berlin Heidelberg: Berlin, Heidelberg, 1983; pp 147−204.

(29) Yoon, D.; Jeong, D.; Lee, H.-J.; Saito, R.; Son, Y.-W.; Lee, H. C.; Cheong, H. Fano resonance in Raman scattering of graphene. *Carbon* **2013**, *61*, 373−378.

(30) Swatek, P.; Wu, Y.; Wang, L.-L.; Lee, K.; Schrunk, B.; Yan, J.; Kaminski, A. Gapless Dirac surface states in the antiferromagnetic topological insulator $MnBi_2Te_4$. *Phys. Rev. B: Condens. Matter Mater. Phys.* **2020**, *101*, 161109.

(31) Lüpke, F.; Pham, A. D.; Zhao, Y.-F.; Zhou, L.-J.; Lu, W.; Briggs, E.; Bernholc, J.; Kolmer, M.; Ko, W.; Chang, C.-Z.; Ganesh, P.; Li, A.-P. *Local manifestations of thickness dependent topology and axion edge state in topological magnet $MnBi_2Te_4$*. arXiv (*Condensed Matter - Mesoscale and Nanoscale Physics*), 2021. arXiv:2101.08247. https://arxiv.org/abs/2101.08247 (accessed 2021-06-29).

(32) Molina-Sánchez, A.; Wirtz, L. Phonons in single-layer and few-layer MoS_2 and WS_2. *Phys. Rev. B: Condens. Matter Mater. Phys.* **2011**, *84*, 155413.

(33) Lee, J.; Ko, T. Y.; Kim, J. H.; Bark, H.; Kang, B.; Jung, S.-G.; Park, T.; Lee, Z.; Ryu, S.; Lee, C. Structural and Optical Properties of Single- and Few-Layer Magnetic Semiconductor $CrPS_4$. *ACS Nano* **2017**, *11*, 10935−10944.

(34) Lee, C.; Yan, H.; Brus, L. E.; Heinz, T. F.; Hone, J.; Ryu, S. Anomalous Lattice Vibrations of Single- and Few-Layer MoS_2. *ACS Nano* **2010**, *4*, 2695−2700.

(35) Osterhoudt, G. B.; Wang, Y.; Garcia, C. A. C.; Plisson, V. M.; Gooth, J.; Felser, C.; Narang, P.; Burch, K. S. Evidence for Dominant Phonon-Electron Scattering in Weyl Semimetal WP_2. *Phys. Rev. X* **2021**, *11*, 011017.

(36) Reedyk, M.; Crandles, D. A.; Cardona, M.; Garrett, J. D.; Greedan, J. E. Raman scattering in the $RTiO_3$ family of Mott-Hubbard insulators. *Phys. Rev. B: Condens. Matter Mater. Phys.* **1997**, *55*, 1442−1448.

(37) Jin, F.; Wang, L.; Zhang, A.; Ji, J.; Shi, Y.; Wang, X.; Yu, R.; Zhang, J.; Plummer, E. W.; Zhang, Q. Raman interrogation of the ferroelectric phase transition in polar metal $LiOsO_3$. *Proc. Natl. Acad. Sci. U. S. A.* **2019**, *116*, 20322−20327.

(38) Zhang, K.; Wang, T.; Pang, X.; Han, F.; Shang, S.-L.; Hung, N. T.; Liu, Z.-K.; Li, M.; Saito, R.; Huang, S. Anisotropic Fano resonance in the Weyl semimetal candidate LaAlSi. *Phys. Rev. B: Condens. Matter Mater. Phys.* **2020**, *102*, 235162.

(39) Klemens, P. G. Anharmonic Decay of Optical Phonons. *Phys. Rev.* **1966**, *148*, 845−848.

(40) Buchenau, S.; Scheitz, S.; Sethi, A.; Slimak, J. E.; Glier, T. E.; Das, P. K.; Dankwort, T.; Akinsinde, L.; Kienle, L.; Rusydi, A.; Ulrich, C.; Cooper, S. L.; Rübhausen, M. Temperature and magnetic field dependent Raman study of electron-phonon interactions in thin films of Bi_2Se_3 and Bi_2Te_3 nanoflakes. *Phys. Rev. B: Condens. Matter Mater. Phys.* **2020**, *101*, 245431.

(41) Xu, B.; Dai, Y. M.; Zhao, L. X.; Wang, K.; Yang, R.; Zhang, W.; Liu, J. Y.; Xiao, H.; Chen, G. F.; Trugman, S. A.; Zhu, J.-X.; Taylor, A. J.; Yarotski, D. A.; Prasankumar, R. P.; Qiu, X. G. Temperature-

tunable Fano resonance induced by strong coupling between Weyl fermions and phonons in TaAs. *Nat. Commun.* **2017**, *8*, 14933.

(42) Coulter, J.; Osterhoudt, G. B.; Garcia, C. A. C.; Wang, Y.; Plisson, V. M.; Shen, B.; Ni, N.; Burch, K. S.; Narang, P. Uncovering electron-phonon scattering and phonon dynamics in type-I Weyl semimetals. *Phys. Rev. B: Condens. Matter Mater. Phys.* **2019**, *100*, 220301.

(43) Tian, Y.; Gray, M. J.; Ji, H.; Cava, R. J.; Burch, K. S. Magneto-elastic coupling in a potential ferromagnetic 2D atomic crystal. *2D Mater.* **2016**, *3*, 025035.

(44) Deng, Y.; Yu, Y.; Song, Y.; Zhang, J.; Wang, N. Z.; Sun, Z.; Yi, Y.; Wu, Y. Z.; Wu, S.; Zhu, J.; Wang, J.; Chen, X. H.; Zhang, Y. Gate-tunable room-temperature ferromagnetism in two-dimensional Fe_3GeTe_2. *Nature* **2018**, *563*, 94−99.